Geophysical Journal International

Geophys. J. Int. (2019) **219,** 911–923
Advance Access publication 2019 July 25
GJI Seismology

doi: 10.1093/gji/ggz332

Slip distribution of the 2017 M_w6.6 Bodrum–Kos earthquake: resolving the ambiguity of fault geometry

A. Ozgun Konca [1], Sezim Ezgi Guvercin,[1] Seda Ozarpaci [2], Alpay Ozdemir,[2] Gareth J. Funning [3], Ugur Dogan,[2] Semih Ergintav,[4] Michael Floyd [5], Hayrullah Karabulut[1] and Robert Reilinger[5]

[1] *Department of Geophysics, Kandilli Observatory and Earthquake Research Institute, Bogazici University, 34684 Istanbul, Turkey. E-mail: ozgun.konca@boun.edu.tr*
[2] *Department of Geomatic Engineering, Yildiz Technical University, 34220 Istanbul, Turkey*
[3] *Department of Earth Sciences, UC Riverside, Riverside, 92521 CA, USA*
[4] *Department of Geodesy, Kandilli Observatory and Earthquake Research Institute, Bogazici University, 34684 Istanbul, Turkey*
[5] *Department of Earth, Atmospheric and Planetary Sciences, Massachusetts Institute of Technology, Cambridge, 02139 MA, USA*

Accepted 2019 July 18. Received 2019 July 12; in original form 2019 March 4

SUMMARY

The 2017 July 20, M_w6.6 Bodrum–Kos earthquake occurred in the Gulf of Gökova in the SE Aegean, a region characterized by N–S extension in the backarc of the easternmost Hellenic Trench. The dip direction of the fault that ruptured during the earthquake has been a matter of controversy where both north- and south-dipping fault planes were used to model the coseismic slip in previous studies. Here, we use seismic (seismicity, main shock modelling, aftershock relocations and aftershock mechanisms using regional body and surface waves), geodetic (GPS, InSAR) and structural observations to estimate the location, and the dip direction of the fault that ruptured during the 2017 earthquake, and the relationship of this event to regional tectonics. We consider both dip directions and systematically search for the best-fitting locations for the north- and south-dipping fault planes. Comparing the best-fitting planes for both dip directions in terms of their misfit to the geodetic data, proximity to the hypocenter location and Coulomb stress changes at the aftershock locations, we conclude that the 2017 earthquake ruptured a north-dipping fault. We find that the earthquake occurred on a 20–25 km long, ∼E–W striking, 40° north-dipping, pure normal fault with slip primarily confined between 3 and 15 km depth, and the largest slip exceeding 2 m between depths of 4 and 10 km. The coseismic fault, not mapped previously, projects to the surface within the western Gulf, and partly serves both to widen the Gulf and separate Kos Island from the Bodrum Peninsula of SW Anatolia. The coseismic fault may be an extension of a mapped, north-dipping normal fault along the south side of the Gulf of Gökova. While all of the larger aftershocks are consistent with N–S extension, their spatially dispersed pattern attests to the high degree of crustal fracturing within the basin, due to rapid trenchward extension and anticlockwise rotation within the southeastern Aegean.

Key words: Satellite Geodesy; Europe; Earthquake source observations; Seismicity and tectonics.

1 INTRODUCTION

On 2017 June 20, an M_w6.6 earthquake struck between the Bodrum Peninsula of southeast Turkey and Kos Island, Greece, in the easternmost Aegean Sea (Fig. 1). The earthquake caused the deaths of two people and injured hundreds, and produced significant structural damage in Bodrum and Kos Island. In addition, the earthquake induced a local tsunami with wave heights reaching 1.4 m (Heidarzadeh *et al.* 2017; Yalçıner *et al.* 2017). Source mechanisms show that the earthquake ruptured an E–W trending normal fault (Table 1), which is consistent with the general N–S extension in the SE Aegean region that is responsible for the opening of the Gulf of Gökova (Fig. 1; see also McClusky *et al.* 2000, Fig. 7).

The initial finite-fault models of the earthquake based on GPS coseismic offsets assumed that the earthquake ruptured a south-dipping normal fault based in part on reported uplift along the Bodrum coast (Saltogianni *et al.* 2017; Tiryakioğlu *et al.* 2017).

© Crown copyright 2019. This article contains public sector information licensed under the Open Government Licence v3.0 (http://www.nationalarchives.gov.uk/doc/open-government-licence/version/3/).

Downloaded from https://academic.oup.com/gji/article/219/2/911/5538783 by Yildiz Teknik University Library (YTU) user on 25 February 2022

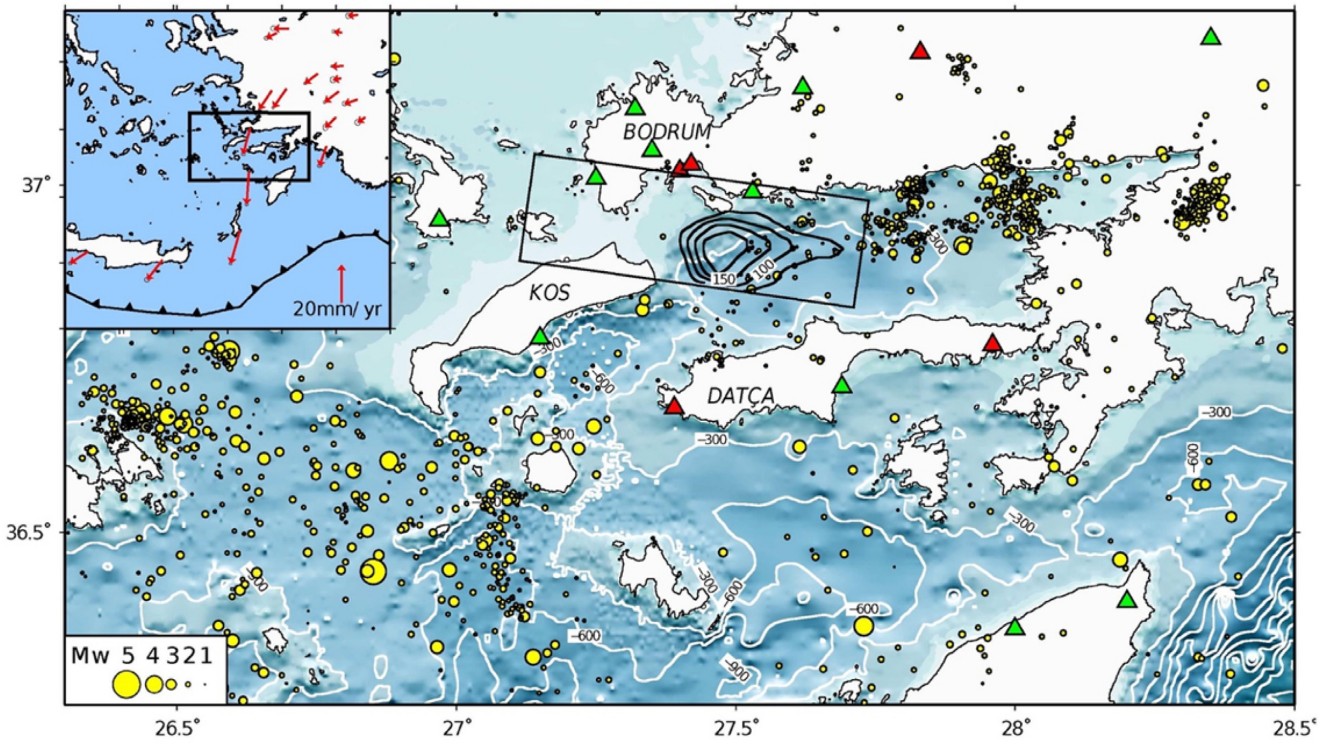

Figure 1. (Inset) Broader study area including the Hellenic Arc and the Aegean Sea region. The red vectors show selected annual GPS velocities with respect to Anatolia (Vernant *et al.* 2014). The black box shows the area of the main figure. (Main Figure) The study region of the 2017 Bodrum–Kos earthquake. The black circles filled with yellow show the seismicity between 2002 and 2008 (Bohnhoff *et al.* 2004; Brüstle 2012) with magnitude scale on the bottom left. The GPS stations used in this study are shown by the green and red triangles for continuous and campaign sites, respectively. The black box represents the boundary of the best-fitting fault plane used for finite-fault modelling, and the black enclosed curves show 50 cm slip contours for the best-fitting north-dipping slip model.

Table 1. Several point source mechanism solutions by global and local agencies.

	NP1 (stk°/dip°/rake°)	NP2(stk°/dip°/rake°)
Global CMT	278/36/-82	88/55/-96
AFAD	275/38/-80	82/53/-98
USGS	285/39/-73	84/53/-103
KOERI	286/53/-72	78/40/-112

AFAD: Disaster and Emergency Management Presidency (AFAD Turkey)
USGS: United States Geological Survey
KOERI: Bogazici University Kandilli Observatory And Earthquake Research Institute

Other studies of the 2017 earthquake that included both GPS and InSAR observations showed significant negative displacement in the line-of-sight (LOS) direction from InSAR data on a small island called Karaada south of the Bodrum coastline, which can be explained by a 40°, north-dipping fault plane (Ganas *et al.* 2017). Later studies by Karasözen *et al.* (2018) and Ganas *et al.* (2019), based on horizontal GPS and InSAR data as well as aftershock distribution, also reported that the rupture occurred on a north-dipping fault.

This ambiguity of fault dip direction arises from two complicating factors. First, normal fault earthquakes can generate quite symmetric patterns of surface displacement in both horizontal and vertical directions, especially when the fault dip angle is close to 45° and the rupture does not reach the surface. Supporting Information Fig. S1 shows a synthetic example, where slip is imposed on a 40° dipping normal fault (See Supporting Information Fig. S1 caption for the details of the synthetic example). The resulting static displacements show that horizontal displacements are quite similar on either side of the fault. There is an uplift both on the footwall side and on the hanging wall side beyond the hinge line. A second factor that contributes to the debate is that the aftershocks of the 2017 earthquake do not clearly show a preferred dip direction. They are distributed over a wide zone that makes it harder to differentiate the fault plane from the auxiliary plane.

The structural evidence whether the south-dipping or north-dipping faults are the main cause of the extension around the 2017 earthquake area is also debated. Kurt *et al.* (1999) investigated the shallow structure of Gulf of Gökova using multichannel seismic data. The reflection profiles along eastern gulf show that there are multiple horst and graben structures. On the other hand, in the western part of the gulf, where the 2017 earthquake struck, there are several south-dipping faults with surface expressions towards the north of the Gulf and one major north-dipping fault with significant vertical offset, named the Datça fault by the authors (Fig. 2). A more recent study of the Gulf of Gökova based on multichannel seismic reflection (Ocakoğlu *et al.* 2018) argued that the south-dipping faults with surface expressions on the northern edge of the Gulf are dominant, while the faults with surface expressions in the south are mostly oblique, left-lateral faults. On this basis, the authors suggest that the 2017 earthquake possibly broke a south-dipping fault.

Downloaded from https://academic.oup.com/gji/article/219/2/911/5538783 by Yildiz Teknik University Library (YTU) user on 25 February 2022

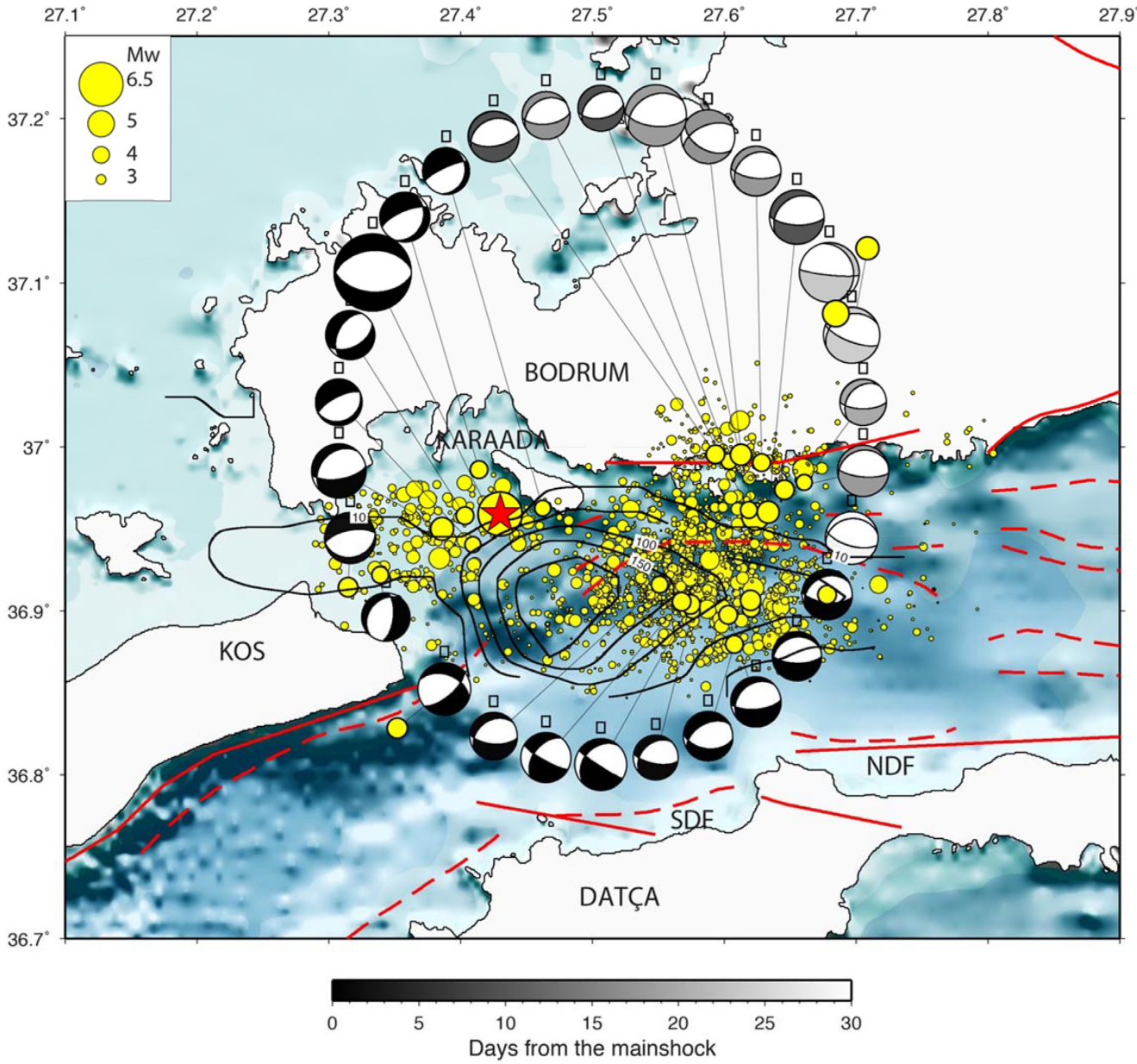

Figure 2. Map view of relocated main shock, aftershock distribution and focal mechanisms. Focal mechanisms are coloured in the grey scale by their occurrence time and scaled in size by magnitude. The yellow circles show the epicentres of aftershock activity of the first 20 d in the vicinity of the main shock (M > 1). The outermost black contour outlines the fault area that slips more than 10 cm. The other black enclosed curves show slip contours at every 50 cm for the final north-dipping slip model. The solid red lines indicate active faults in the region from active fault map of General Directorate of Mineral Research and Exploration (Emre *et al.* 2013), while the red dashed lines indicate faults from the study of Görür *et al.* (1995) and Kurt *et al.* (1999). The tick marks show the hanging wall of the identified normal faults from Kurt *et al.* (1999). SDF: South Datça Fault, NDF: North Datça Fault.

Given various conflicting interpretations of the dip direction of the 2017 earthquake fault, we explore models for coseismic fault geometry and slip distribution for both north- and south-dipping faults. In order to find the best-fitting north- and south-dipping fault planes, we perform a grid search, where finite-fault models are generated centred at every grid point for both possible fault planes, using ascending and descending orbit InSAR data, and GPS estimates of horizontal and vertical coseismic displacements. We show that adding the vertical GPS displacements to the horizontal GPS and InSAR data provides sufficient constraints to differentiate between the two possible fault planes. Next, we compare the location of the hypocenter and aftershock locations with respect to the fault plane. We also determined the mechanism of the larger aftershocks following the main shock, and compare the stress perturbations of the best-fitting north- and south-dipping fault planes to aftershock locations. The results of our study strongly support a north-dipping coseismic fault for the 2017 Bodrum–Kos earthquake.

Downloaded from https://academic.oup.com/gji/article/219/2/911/5538783 by Yildiz Teknik University Library (YTU) user on 25 February 2022

2 TECTONIC SETTING

The Gulf of Gökova, where the 2017 Earthquake was located, is an ∼E–W striking, extensional graben lying in the backarc of the Hellenic subduction zone where it 'abuts' southwest Anatolia (Fig. 1). The Gulf is part of the Western Anatolia Extension Province that extends from the eastern Hellenic Trench north at least as far as the Izmir Peninsula and the Gediz and Buyuk Menderes Graben systems (e.g. Sengor *et al.* 1984). The present-day rate of N–S extension across this region is about 20 mm yr^{-1} (McClusky *et al.* 2000; Aktug *et al.* 2009; Floyd *et al.* 2010), with ∼ 4 mm yr^{-1} across the Gulf of Gökova proper (Fig. 1), or 20 per cent of the total rate of extension. This high degree of extension is responsible for the large number of M > 5 historic earthquakes that have occurred in the Gulf.

Structural studies indicate two phases of deformation in the Gulf region: During the Late Miocene, a phase of N–S compression and E–W extension, and the more recent Pliocene N–S extension that formed the present-day morphology of the Gulf, (e.g. Görür *et al.* 1995; Gurer *et al.* 2013). We note that a Pliocene initiation of N–S extension is consistent with the present-day rate of extension across the Gulf (∼4 mm yr^{-1}, Fig. 1), and width of the Gulf (∼20 km), providing an age estimate of ∼ 5 Ma.

The underlying causes for these two phases of deformation are debated, but it is generally agreed that the initial compressive phase was associated with collision of the Hellenic–Cyprus arc system with Anatolia, followed in the Pliocene by N–S extension and anticlockwise rotation induced by retreat of the Hellenic Trench (e.g. Sengor *et al.* 1984; Royden and Papanikolaou 2011). The rotation of Late Miocene faults and dissection by younger, and presently active, E–W normal faults results in the complex system of faults that accommodate extension across the Gulf. The broadly distributed aftershocks of the 2017 earthquake (Fig. 2) are consistent with this high degree of faulting.

Present-day morphology of the Gulf results from faulting on a set of normal fault segments (Fig. 2) with the most prominent being the south-dipping, North Datça Fault system lying along the northern side of the Gulf, and the north-dipping, South Datça Fault system along the southern shoreline (Görür *et al.* 1995; Emre *et al.* 2013). On a more detailed scale, Kurt *et al.* (1999), investigated the shallow structure of the Gulf using multichannel seismic data. The reflection profiles along the eastern Gulf show multiple horst and graben structures aligned more or less east–west (Fig. 2). In the western Gulf, where the 2017 earthquake struck, there are several south-dipping faults on the north side (Ocakoğlu *et al.* 2018), and the north-dipping Datça Fault in the southern Gulf. Given the absence of an observed surface break, and the complexity and limited available information on faulting in the Gulf, the structural evidence for constraining the location and source of the 2017 coseismic fault is at best equivocal (e.g. Sengor *et al.* 1984; Royden & Papanikolaou 2011).

3 DATA AND METHODS

3.1 GPS data

In this study, 12 continuous stations and 5 campaign GPS sites were used for the modelling of coseismic slip distribution. While many of the survey sites and continuous GPS stations (Supporting Information Tables S1A and S1B, respectively) were present in the area before the Bodrum–Kos earthquake, most of them are on the Bodrum Peninsula (Fig. 1). Five continuous GPS stations (TRKB, MUMC, ORTA, TGRT and YALI) are compiled from the network of the Association of Bodrum Geomatic Engineers (BODRUM-CORS), three stations (DATC, DIDI and MUG1) are part of the Continuously Operating Reference Stations, Turkey (CORS-TR) and four stations (086A, 087A, KALY and RODO) from NOANET in Greece (Fig. 1). Daily time-series of 11 continuous GPS stations are shown in Supporting Information Fig. S2.

In addition to the continuous data, we added five campaign sites to the analysis. The observations before the earthquake for the campaign sites were purchased from the General Directorate of Mapping, and the campaign sites were measured after the earthquake as part of this study.

The precise coordinates of the stations and secular velocity estimates were determined using GAMIT/GLOBK (10.6) software (Herring 1998; Herring *et al.* 2015). To estimate the coseismic displacements of campaign sites, we used a simple, linear model for the elastic strain accumulation to extrapolate the site position to the time immediately preceding the shock. We used the velocity field from Reilinger *et al.* (2006) to identify the pre-earthquake secular motions of campaign sites. Similarly, we used the same strategy to extrapolate positions measured after the earthquake back to the time immediately after the main shock. The resulting coseismic displacements from survey sites are listed in Supporting Information Table S1A.

For the continuous stations, we used 2 d of observations before and after the earthquake (except MUMC) to estimate the coseismic displacements directly. MUMC had a problem before the earthquake (2017 February 9) and was re-activated after the earthquake (27 July). The pre-earthquake position of MUMC was extrapolated from the station time-series. The coseismic displacements for continuous GPS sites are tabulated in Supporting Information Table S1B.

Table 2. Details of Sentinel-1 InSAR data used in this study.

Track	Frame	Geom.	Subsw.	Date 1	Date 2	Baseline
131	114–119	asc.	1–2	2017/07/12	2017/07/24	−37 m
036	467–472	desc.	1–2	2017/07/12	2017/07/24	−5 m

3.2 InSAR data

The epicentral region of the Bodrum–Kos earthquake is covered by both ascending and descending tracks of the Copernicus/ESA Sentinel-1 satellite mission (Supporting Information Fig. S3), and multiple acquisitions were made in the days and weeks following the event. We processed a selection of coseismic pairs of SAR images from both tracks into interferograms using the JPL/NASA ISCE software (Rosen *et al.* 2011; Gurolla *et al.* 2016), with a 30 m-resolution deformation model from the Shuttle Radar Topography Mission (Farr *et al.* 2007) used to mitigate topographic artefacts. Selecting for the lowest levels of tropospheric noise present in each interferogram, assessed by visual inspection, we choose one ascending pair and one descending pair for further analysis (Table 2). We unwrap these interferograms using the SNAPHU algorithm (Chen & Zebker 2002), and manually fix any unwrapping errors by isolating areas with anomalous phase (i.e. which do not match the phase of adjacent areas) and shifting them by multiples of 2π.

The original interferograms and the unwrapped range changes are shown for both tracks in Supporting Information Fig. S3. The interferograms both have a high level of interferometric correlation on land and in the area surrounding the epicentre. The largest deformation gradients are located on the island of Karaada (Fig. 2;

Downloaded from https://academic.oup.com/gji/article/219/2/911/5538783 by Yildiz Teknik University Library (YTU) user on 25 February 2022

Table 3. The velocity model for the region obtained from earthquake relocations.

Depth (km)	Vp (km s^{-1})	Vs (km s^{-1})
0.0	3.15	1.73
2.0	4.84	2.77
4.0	5.40	3.09
6.0	5.71	3.28
8.0	5.85	3.36
10.0	6.02	3.46
12.0	6.13	3.51
16.0	6.20	3.56
20.0	6.50	3.75
30.0	7.38	4.25
37.0	7.85	4.33

Supporting Information Fig. S3a), approximately 5 km south of Bodrum; both interferograms show positive range change of ∼15–20 cm with respect to the Turkish mainland at the southern tip of Karaada, indicating that it subsided coseismically. To prepare the data for modelling, we applied a curvature-based quadtree decomposition (e.g. Simons *et al.* 2002) focusing data sampling on features of interest in the data and reducing the number of data points in each interferogram from ∼9 million to ∼300.

3.3 Aftershock relocation

We relocated the main shock and aftershocks during the first 20 d following the main shock using the catalogues of the General Directorate of Disaster Affairs of Turkey (AFAD), and Bogazici University Kandilli Observatory (KOERI) Regional Earthquake-Tsunami Monitoring Center (BDTIM) (see Supporting Information Fig. S4 for the station distribution map). For the earthquakes that exist in both catalogues (AFAD and BDTIM), phase readings were merged. The earthquakes that existed only in one of the catalogues were also included in the joint catalogue.

We revised the phase pickings using the continuous waveforms for the first 10 d (∼1500 events) and used the phase pickings from the catalogues for the later days. The final presented catalogue contains 2900 events between 2017 July 20 and August 7. The epicentral distribution is shown in Fig. 2 and in Supporting Information Fig. S5 for various time windows.

We relocated the earthquakes using the HYP program that is part of SEISAN Earthquake Analysis Software (Ottemöller *et al.* 2013), which is based on Lienert *et al.* (1986). A 1-D velocity model was computed using the VELEST inversion code that minimizes traveltime errors (Kissling *et al.* 1994; Table 3). The obtained *P* wave model is similar to the one obtained by Akyol *et al.* (2006) for southwest Turkey from earthquake relocations. The deviations from the 1-D velocity model are accounted for in the station corrections. Average location uncertainties are shown in Supporting Information Fig. S6. The mean horizontal uncertainties are ∼1.0 and ∼1.8 km for latitude and longitude, respectively (Supporting Information Fig. S6 a–b). The mean of the depth uncertainty is ∼3 km with most events within the 2 and 4 km range (Supporting Information Fig. S6c). The magnitude completeness threshold of the catalogue is estimated as ∼2.0 and the b-value is 1.1 (Supporting Information Fig. Sd).

3.4 Aftershock mechanisms

The mechanisms of aftershocks were studied using a subset from 83 broad-band stations of Kandilli Observatory and Research Institute (KOERI), AFAD, German Research Center (GFZ), Italian Seismic Network (INGV), Seismological Network of Crete and Hellenic Unified Seismic Network (HUSN). For the inversion of the fault plane solutions, we used the Generalized Cut and Paste code by (Zhu & Helmberger 1996; Zhu & Ben-Zion 2013). The method relies on filtering and shifting of two components of P_{nl} waveform windows and three components of the *S* and surface waveform windows separately and performing a grid search to find the earthquake mechanism and magnitude (Zhu & Ben-Zion 2013). Green's functions were calculated using the velocity model from earthquake relocations (Table 3).

Source mechanisms of 29 earthquakes in the range of M_w 4–M_w6.6, including the main shock, were obtained and are tabulated in Table 4. We fixed the latitude and longitude of the earthquakes from our revised catalogue. In addition to the best-fitting mechanisms, we performed a centroid depth grid search in order to determine the centroid depth. The calculated centroid depths are consistent with the relocated catalogue within an uncertainty of around ±1 km (See Supporting Information Fig. S7 caption for the details of the waveform inversion and Supporting Information Fig. S7 for an example of waveform fits). For some events with M > 4, it was not possible to model the earthquakes due to waveform complexity. Especially in the first few hours following the main shock, the high seismic activity rate leads to interference of waves coming from different earthquakes that occur very close in time, making waveform modelling impossible.

In order to assess the uncertainties associated with the obtained source mechanisms, we performed a bootstrap analysis for 3 of the 29 earthquakes. We selected the events that have variance reduction around 50 per cent, which is typical for this sequence. For each event, 1000 inversions are performed for the mechanism of the earthquakes by random resampling of stations. The results (Supporting Information Fig. S8) show that the uncertainties in the strike, dip and rake values are below 10° and source mechanisms are well resolved.

3.5 Finite-fault inversion

In order to find the slip distribution, we performed an inversion of two tracks of InSAR data as well as the GPS displacements using the finite-fault inversion of Ji *et al.* (2002), which finds a best-fitting solution for the slip on a planar fault by minimizing the error using a simulated annealing algorithm. The error function consists of L_2-norm misfit to the geodetic data weighted based on their 1σ uncertainties and the Laplacian smoothness constraint on the slip distribution. Since we do not have independent error estimates for the InSAR data, we assumed a 1σ uniform uncertainty of 2.0 cm for all resampled InSAR measurements. This specific value was partly chosen in order to keep the weight on the inversion roughly the same for the GPS data and each InSAR track. For the InSAR data, a static offset was added to the inversion parameters in order to account for the unknown zero level in each interferogram. For all the models, the Green's functions were calculated using the 1-D layered model in Table 3.

For the grid-search of best-fitting north- and south-dipping fault planes, we used 13 × 13 sub-faults with sizes of 2.5 km × 1.7 km along strike and dip, respectively. After finding the location of the best-fitting fault planes using the grid search, a wider fault plane was built with 27 and 16 sub-faults with size of 2 km × 1.35 km along strike and dip, respectively, to find the final best-fitting solutions for both dip directions.

Downloaded from https://academic.oup.com/gji/article/219/2/911/5538783 by Yildiz Teknik University Library (YTU) user on 25 February 2022

Table 4. Mechanisms of the main shock and the aftershocks obtained in this study from regional seismic data.

Date	Time	Lat°	Lon°	Depth(km)	M_w	Stk°	Dip°	Rake°
2017/07/20	22.31	36.959	27.43	12	6.48	94	48	−84
2017/07/21	0.15	36.958	27.4033	10	4.09	64	49	−63
2017/07/21	0.52	36.9403	27.4093	10	3.9	66	20	−87
2017/07/21	0.56	36.8796	27.6075	8.6	4.15	96	48	−65
2017/07/21	1.24	36.9625	27.4623	10.5	3.93	245	77	−74
2017/07/21	1.34	36.9055	27.5678	14.2	4.17	119	79	−42
2017/07/21	1.37	36.904	27.5743	9.5	4.34	123	84	−58
2017/07/21	1.49	36.986	27.414	14.1	4.16	247	70	−70
2017/07/21	2.11	36.8285	27.3521	0.5	4.4	291	44	−37
2017/07/21	3.58	36.8976	27.6031	13.9	4.22	85	66	−72
2017/07/21	5.12	36.9016	27.6203	1	4.13	91	67	−84
2017/07/21	5.51	36.922	27.3391	10.3	4.03	220	30	−60
2017/07/21	9.54	36.91	27.678	14.7	4.23	96	64	−74
2017/07/21	17.8	36.95	27.386	12.9	4.53	84	65	−68
2017/07/22	0.33	36.916	27.551	10.2	3.98	94	63	−70
2017/07/22	4.52	36.9	27.576	15.1	3.75	100	67	−62
2017/07/22	17.8	36.9143	27.3148	7.85	4.29	79	25	−90
2017/07/30	7.1	36.9956	27.5933	10.37	4.24	82	59	−81
2017/07/30	10.55	36.9913	27.6035	10.25	3.86	80	54	−73
2017/07/30	17.5	36.9601	27.6333	12.2	4.56	92	66	−71
2017/08/07	5.17	36.9951	27.6128	10.4	4.52	120	49	−50
2017/08/07	5.43	36.9616	27.6188	11.87	4.01	84	60	−77
2017/08/07	18.24	36.9905	27.6285	9.14	4.16	96	66	−71
2017/08/08	1.45	36.9738	27.6458	6.86	4.3	95	71	−83
2017/08/08	7.41	36.9576	27.6236	11.03	5.16	95	61	−72
2017/08/09	22.55	36.9783	27.6608	13.74	3.87	90	67	−66
2017/08/13	11.15	37.0813	27.6848	28	5	346	20	−21
2017/08/14	2.42	37.121	27.7088	7	4.69	111	71	−72
2017/08/18	14.9	36.9063	27.62	16.79	4.41	106	65	−79

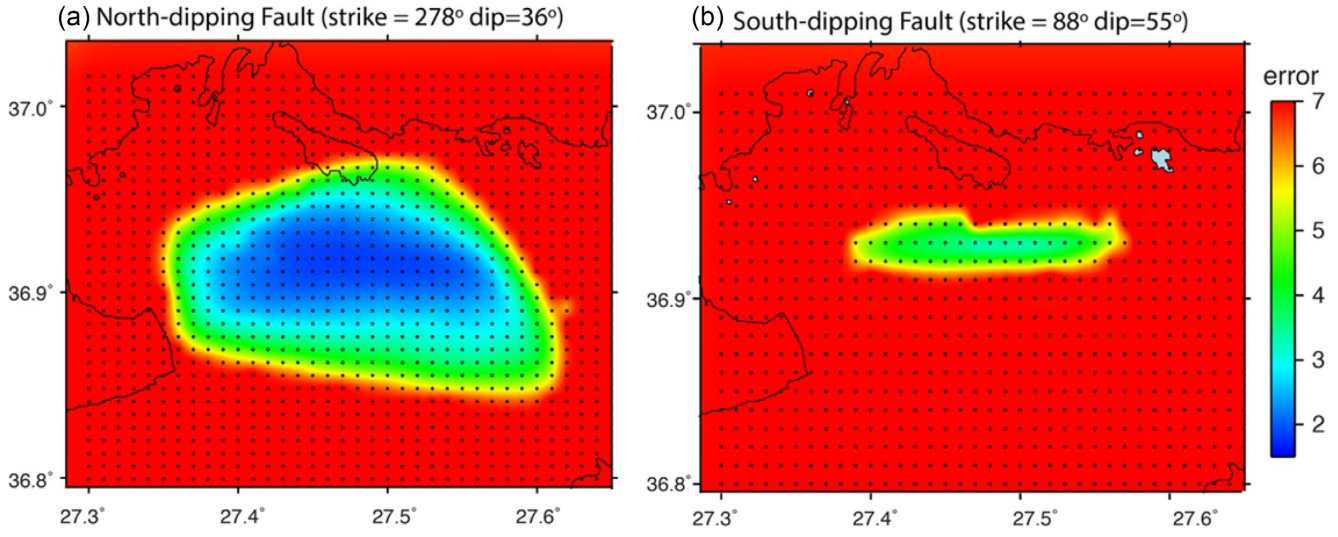

Figure 3. Results of the grid search for finding the location of the best-fitting fault plane for the (a) north-dipping fault planes (strike 278°, dip = 36°) and (b) south-dipping fault plane (strike = 88°, dip = 55°). Each black dot represents a finite-fault model where the location of the dot represents the centre point of the fault plane along strike and 6 km depth .The x_r^2 error values are saturated at 7.0 for both figures (see text for discussion).

4 RESULTS

4.1 Aftershock locations and mechanisms

Fig. 2 shows the epicentre distribution of relocated aftershocks during the first 18 post-earthquake days, and the focal mechanisms of aftershocks obtained from regional waveforms (catalogue available in the Supporting Information). Most aftershocks occurred near the lateral terminations of the 2017 rupture. Supporting Information Fig. S5 shows the time evolution of seismicity during the first 20 d of aftershocks. The early aftershocks surround the highest slipping region. In the following day, the aftershock activity propagates in every direction and significant activity can be observed both towards the east and west. The cumulative activity shows that the 2017 earthquake triggered seismicity on fault systems as far as 40 km north of the coseismic fault (Fig. 2; Supporting Information Fig. S5).

Downloaded from https://academic.oup.com/gji/article/219/2/911/5538783 by Yildiz Teknik University Library (YTU) user on 25 February 2022

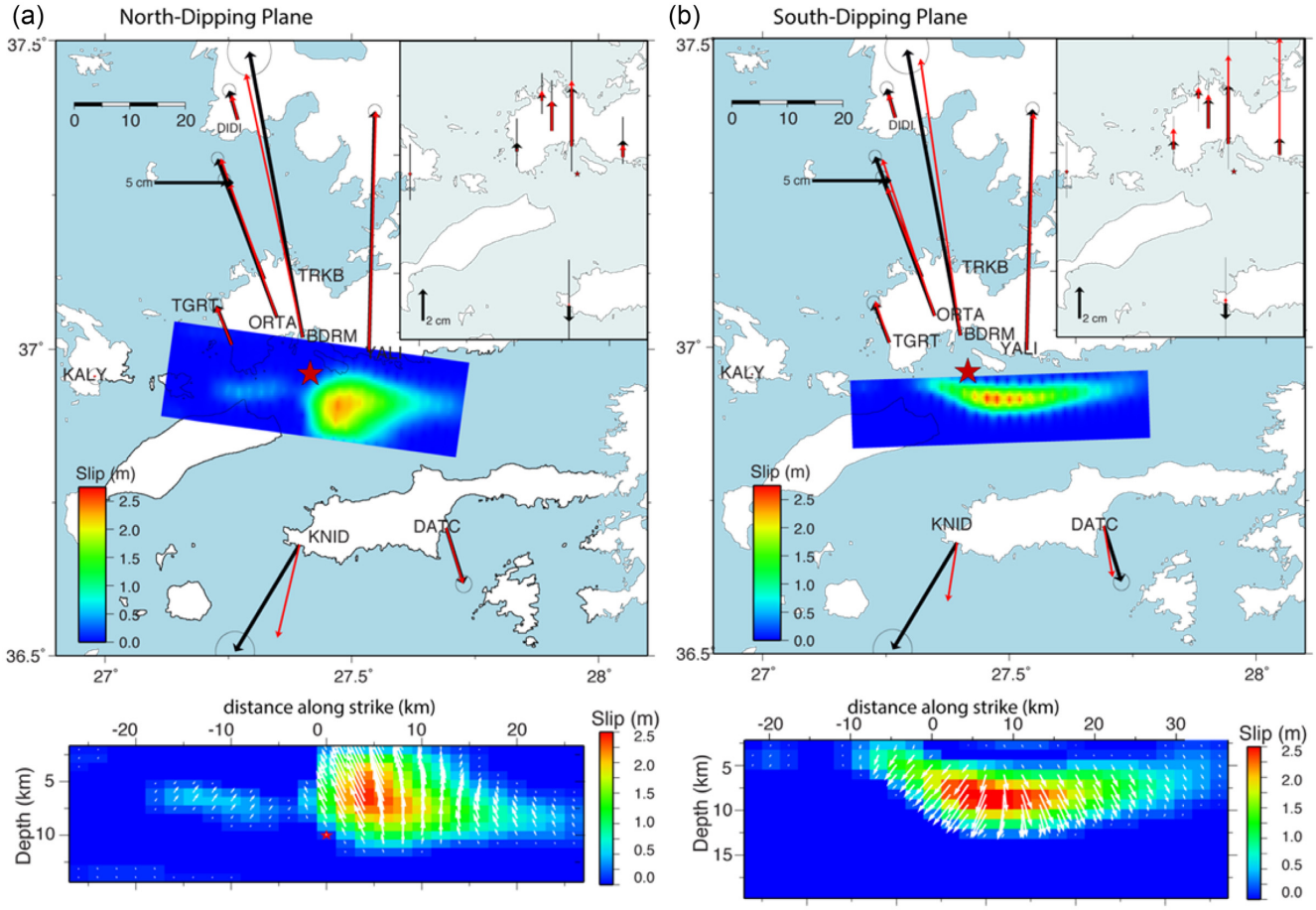

Figure 4. (a) (Top) Map view of slip distribution and horizontal GPS offsets (the black arrows) and model predictions (the red arrows) for the best-fitting north-dipping fault. The inset shows the fits to the vertical GPS data. Coseismic uplift is shown by a vector pointing up and the vertical errors are shown by the black bars. The red star shows the epicentre location from this study. (Bottom) Fault plane view of the slip distribution for the north-dipping fault plane. The hypocenter obtained from relocation is also shown since it projects to the north-dipping plane. (b) Same as (a) for the south-dipping fault plane.

Most aftershock source mechanisms are consistent with N–S extension, similar to the main shock, especially those very close to the main shock slip zone (Fig. 2; Supporting Information Table S3), supporting models using planar fault geometries (e.g. Karasözen *et al.* 2018). However, there are some oblique mechanisms with small strike-slip components, and some earthquakes with different orientations, including near the northwestern end of the rupture area where we find several NE–SW striking normal fault mechanisms. This change in orientation possibly marks the western end of the fault that ruptured during the 2017 event, consistent with fault maps that show a more NE–SW fault further west (Fig. 2).

4.2 Grid search for the best-fitting fault plane location

As a first step of identifying the geometry of the earthquake fault, we performed a grid search to find the best-fitting fault plane location using both the north- and south-dipping planes. For the strike and dip, we chose the Global CMT solution (Table 1). However, we also repeated the test using the USGS solution to show that our result is not dependent on small differences in strike and dip values. For each grid search point, we build a finite fault and invert for the slip distribution using the geodetic data.

The model misfit is quantified by the sum of reduced chi-squared (χ_r^2) error of GPS data and two tracks of InSAR data:

$$\chi_r^2 = \frac{1}{N_{GPS}} \sum_{i=1}^{N_{GPS}} \left(\frac{d^i - s^i}{\sigma_i} \right)^2 + \frac{1}{N_{InSAR1}} \sum_{i=1}^{N_{InSAR1}} \left(\frac{d^i - s^i}{\sigma_i} \right)^2 + \frac{1}{N_{InSAR2}} \sum_{i=1}^{N_{InSAR2}} \left(\frac{d^i - s^i}{\sigma_i} \right)^2, \quad (1)$$

where d^i and s^i are the ith data and model predictions, respectively. σ_i is the standard deviation of the ith data point, and N represents the number of data points for each three data sets.

Fig. 3 shows the grid search for the best-fitting location for the fault plane for the north- and south-dipping planes, where every finite-fault model is represented by a grid point in the middle point the fault plane at a depth of 6 km, and colour represents the error of the finite-fault inversion as in eq. (1). The grid search results show that while both fault planes can account for the geodetic data, the best-fitting north-dipping fault plane fits the geodetic observations (minimum $\chi_r^2 = 1.82$) better than the south-dipping fault plane (minimum $\chi_r^2 = 3.29$). In addition, there is a wider range of locations that fit the data for the north-dipping plane compared to the south-dipping plane (Fig. 3).

In this study, we did not systematically change the strike and dip while performing the grid-search for finding the best-fitting fault plane location. Instead, we relied on point-source mechanisms to

Downloaded from https://academic.oup.com/gji/article/219/2/911/5538783 by Yildiz Teknik University Library (YTU) user on 25 February 2022

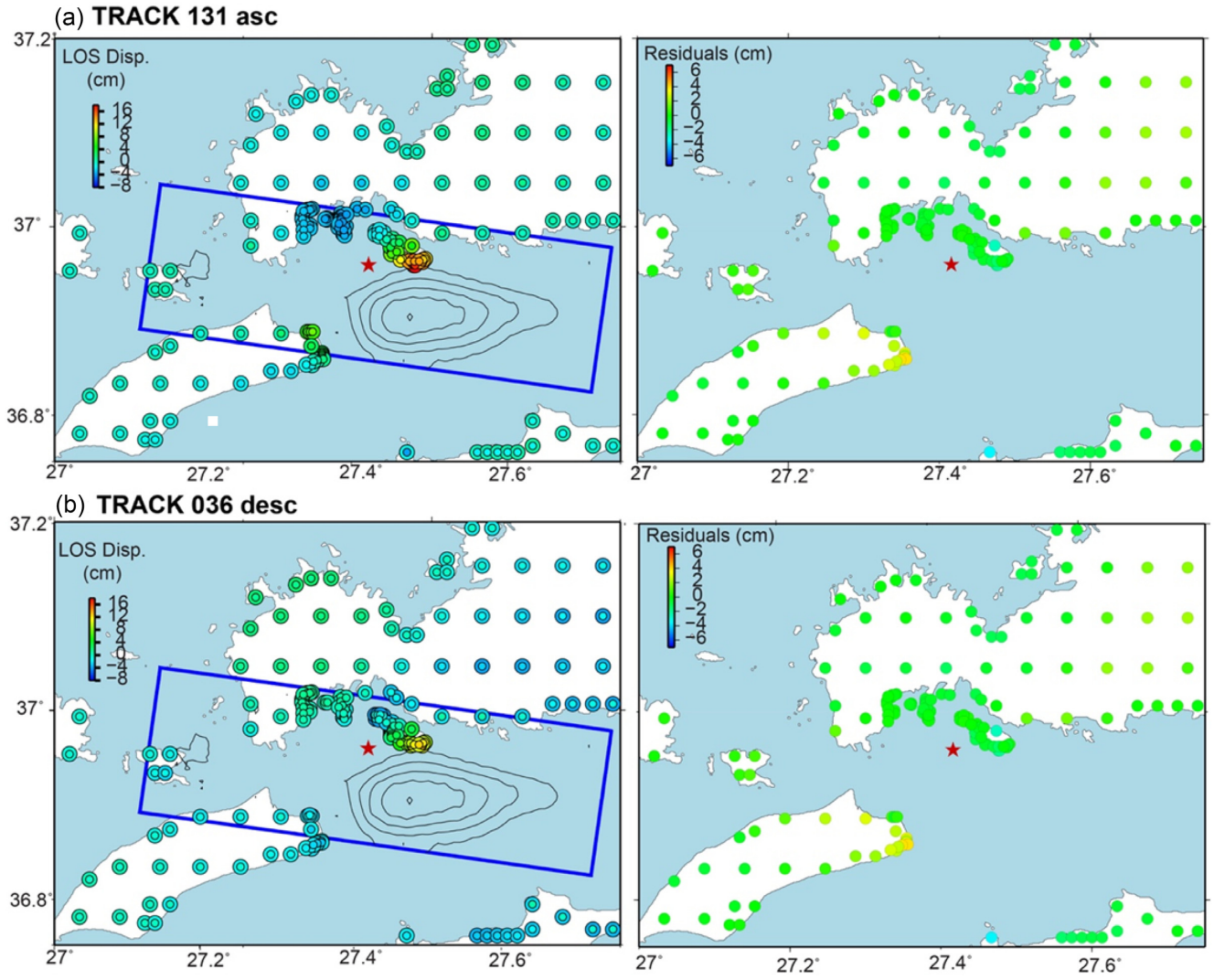

Figure 5. InSAR data for two tracks used in the modelling and the best-fitting north-dipping fault geometry. (a) (Left-hand panel) InSAR data for ascending Track 131 along LOS direction (the outer circles) and the model predictions (the inner circles). The blue rectangle shows the edges of the fault plane, and the black enclosed curves show the 50 cm slip contours of the best-fitting north-dipping slip model. The red star shows the epicentre location of the of the main shock. (Right-hand panel) The residuals for the model (data minus model prediction). The red star shows the epicentre location of the main shock. (b) Same as (a) for the descending Track 036.

fix the strike and dip of the fault plane. However, as mentioned above, we did try the same test using both fault planes based on USGS focal mechanism solution's strike and dip values (Table 1). The results of this test are very similar to those obtained from GCMT-based fault planes (Supporting Information Fig. S9). This result shows that systematic preference of the north-dipping plane is not dependent on the variability of the fault plane strike and dip angles.

4.3 Best-fitting north-dipping and south-dipping slip distributions from finite-fault models

In order to get the final, best-fitting north and south-dipping fault plane solutions, we performed the inversions for both fault planes with wider fault areas with finer sub-faults using their best-fitting location obtained during the grid-search process. The geodetic misfit for the north-dipping plane (GPS $\chi_r^2 = 0.66$, InSAR $\chi_r^2 = 0.31$, 0.44) is still significantly lower than the misfits for the south-dipping fault plane (GPS $\chi_r^2 = 1.61$, InSAR $\chi_r^2 = 0.97$, 0.52), clearly favouring a north-dipping plane.

Fig. 4 shows the slip distribution and the fits to the GPS data for slip models for both dip directions. The slip distributions for both fault geometries show mostly a rupture towards the east. However, the slip model using the south-dipping fault plane indicates a longer rupture (~40 km) compared to the north-dipping plane solution (25 km) and it is less spread out at depth.

Comparison of the model fits to the coseismic GPS displacements shows that the vertical GPS in particular is better fit by the north-dipping model (Fig. 4, inset). The south-dipping slip model overestimates the vertical displacements of the stations to the north of the fault plane, while the horizontal vectors are slightly underestimated. The fits to the InSAR data show that the main difference is the estimation of subsidence on the southeast tip of Karaada (Fig. 5). Specifically, vertical GPS displacements on the Bodrum coast, and the InSAR fringes on the island of Karaada, put tight constraint on the possible solution.

Downloaded from https://academic.oup.com/gji/article/219/2/911/5538783 by Yildiz Teknik University Library (YTU) user on 25 February 2022

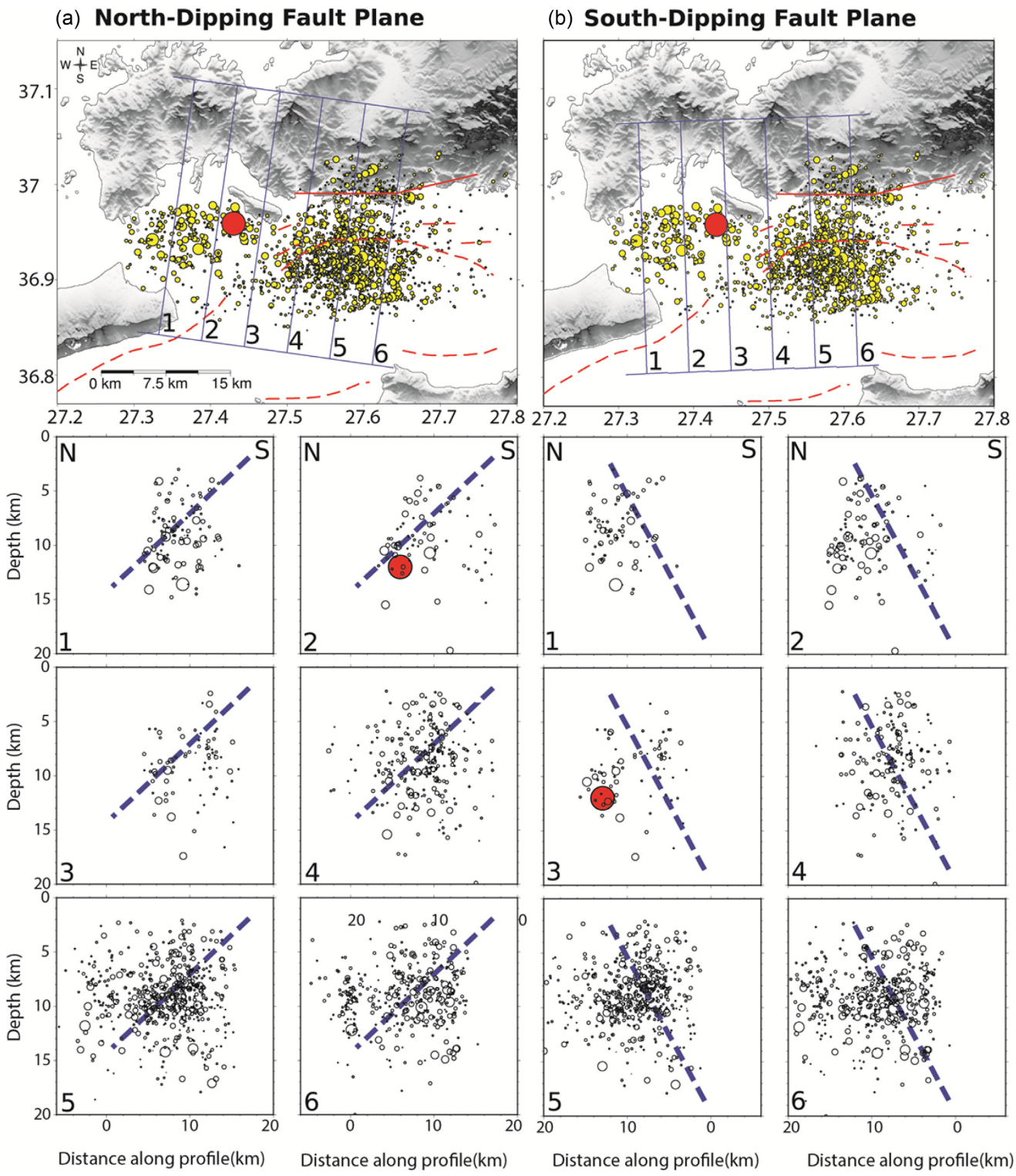

Figure 6. Seismicity distribution of the first 20 d with fault planes dipping to (a) north, and (b) south. The thick dashed lines show the fault plane. The red filled circle shows the location of the main shock from this study. Each profile includes earthquakes within 2.5 km distance to the profile line in each direction. The red dashed lines show the fault lines from Emre *et al.* (2013), Görür *et al.* (1995) and Kurt *et al.* (1999).

Fig. 6 shows the profiles of aftershocks and their geometric relation to the two possible fault plane geometries. On the western profiles, the north-dipping fault plane fits the depth distribution of seismicity better that the south-dipping plane. However, overall the distribution of hypocenters delineates no clear fault plane. Rather, the aftershocks occur throughout a broad (∼100 km) region around the coseismic fault, consistent with the main shock having triggered activity across a complex set of regional faults. As such, the distribution of aftershocks provides few constraints on the dip of the coseismic fault.

Downloaded from https://academic.oup.com/gji/article/219/2/911/5538783 by Yildiz Teknik University Library (YTU) user on 25 February 2022

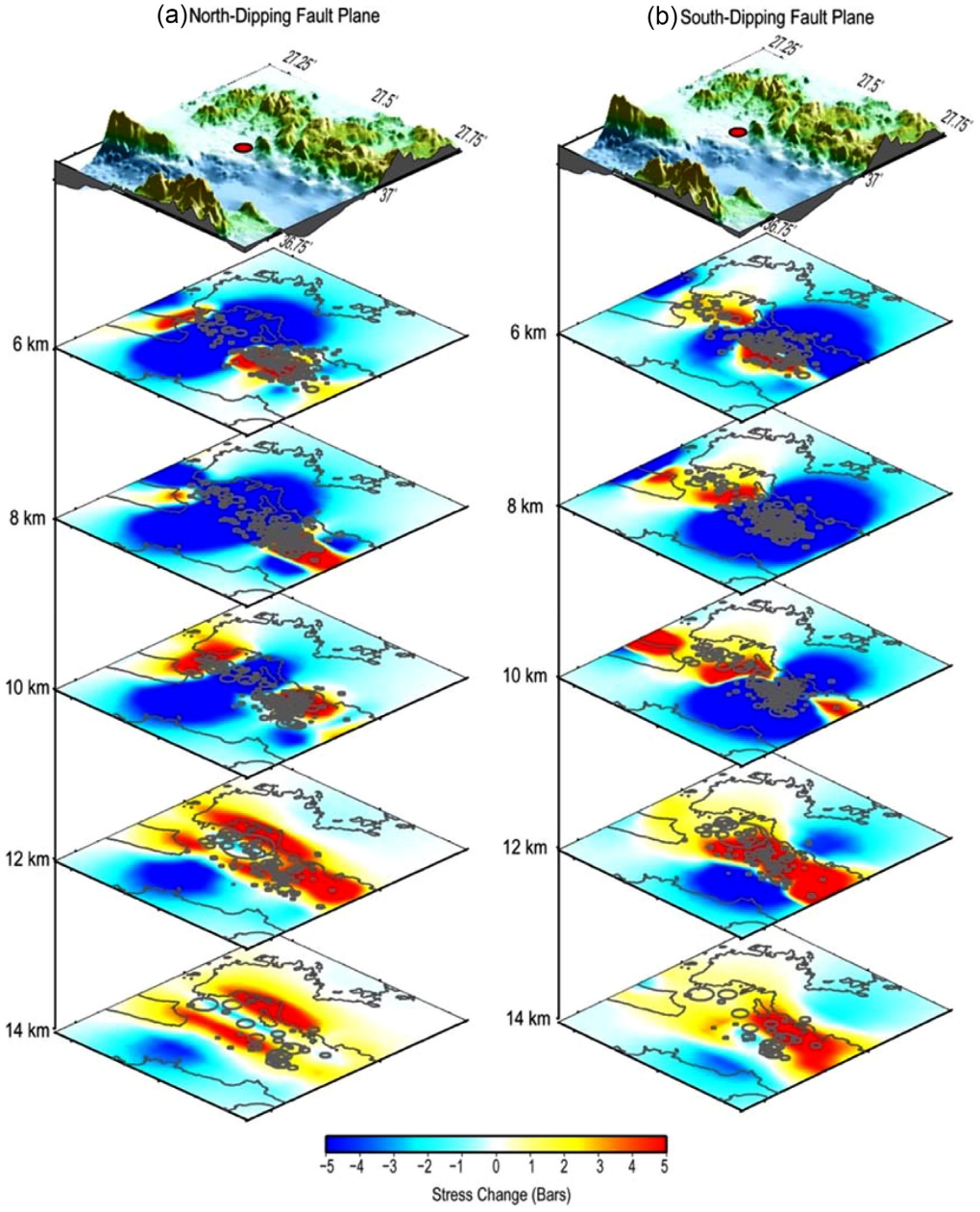

Figure 7. The Coulomb stress changes with the same mechanism as the main shock for the (a) north-dipping (left-hand panel) and (b) south-dipping (right-hand panel) faults at depths between 4 and 14 km. The grey circles show the aftershocks ($M \geq 1$) during the first 5 d following the main shock (between 2017/07/20 and 2017/07/25). Coulomb stress changes are calculated on faults having the same mechanism as the main shock.

On the other hand, the location of the hypocenter is quite consistent with a north-dipping fault (Fig. 6). The perpendicular distance of the hypocenter from the north-dipping fault plane is only 1 km. For the south-dipping plane, the distance of the hypocenter to the fault plane is 5 km, which is on the higher end of our estimation of location errors.

4.4 Coulomb stress changes due to coseismic slip and early aftershock distribution

Although slip models with north and south-dipping fault planes generate similar displacements at geodetic data sites, the variations in slip distributions (Fig. 4) generate different Coulomb stress perturbations at depth. Since the early aftershocks are expected to preferentially cluster in volumes of positive stress changes, the relationship between aftershock locations and stress changes can be used to identify a preferred coseismic model.

Towards this end, we calculated the Coulomb stress change on normal faults with the same mechanism as the main shock, which is the dominant mechanism (Fig. 2). Fig. 7 shows depth slices of Coulomb stress change for the north and south-dipping faults along with the seismicity in that depth $\pm$ 1 km during the first 5 d of aftershocks. The result shows that in the depth range of significant slip (4–10 km) the north-dipping model is more consistent with the seismicity. Especially at the depth slices of 8 and 10 km, the south-dipping model shows significant seismicity at zones of Coulomb stress decrease.

Downloaded from https://academic.oup.com/gji/article/219/2/911/5538783 by Yildiz Teknik University Library (YTU) user on 25 February 2022

5 DISCUSSION

5.1 Dip direction and slip distribution of the 2017 Bodrum–Kos earthquake

As described in the Introduction, the fault geometry of the 2017 Bodrum–Kos earthquake has been a subject of controversy since it occurred. Initial studies of the earthquake (Saltogianni *et al.* 2017; Tiryakioğlu *et al.* 2017) used a south-dipping fault model in order to model the coseismic horizontal displacements. Subsequent studies using horizontal GPS and the InSAR data, along with the main shock and aftershock relocations, argued that the rupture occurred on a north-dipping fault (Karasözen *et al.* 2018; Ganas *et al.* 2019). Ganas *et al.* (2019) systematically searched for the best-fitting south-dipping plane dimensions with constant slip and showed that the InSAR data are better explained by a north-dipping model.

In this study, by including vertical GPS displacements, additional campaign sites to the geodetic data sets, two additional tracks of InSAR data, and by systematically searching for the best-fitting fault plane using a grid search of finite-fault solutions, we obtained the best-fitting finite-fault solutions for both dip directions. Then, we calculated the Coulomb stress change due to coseismic slip for both slip models and compared the stress perturbations to the early aftershock locations.

Our analysis shows that a north-dipping coseismic fault plane provides a better fit to the geodetic data, is more consistent with the independently obtained hypocenter location and accounts better for the expected relationship between aftershock locations and Coulomb stress changes. Critically, the hypocenter location does not agree with the location of the south-dipping fault plane. When a fault plane that passes near the hypocenter is used, a south-dipping fault plane cannot fit the GPS observations. On the basis of these considerations, we conclude that a north-dipping fault ruptured during the 2017 earthquake, supporting the interpretations of Karasözen *et al.* (2018) and Ganas *et al.* (2019).

Our preferred geodetic slip distribution (Fig. 4a) indicates that the earthquake ruptured a 20–25 km long patch towards east of the hypocenter between 2 and 10 km of depth range. The calculated peak slip is more than 2 m. The location of the hypocenter and the slip distribution shows that rupture is primarily to the east of the hypocenter. Our final slip distribution is similar to that reported by Ganas *et al.* (2017) and Karasözen *et al.* (2018).

5.2 Relationship to regional tectonics

The 2017 Bodrum–Kos earthquake was one of many earthquakes that produced the present-day morphology of the Gulf of Gökova. The high rate of Pliocene extension directed towards the eastern Hellenic arc is consistent with the large number of M > 5 historic earthquakes that have occurred in the Gulf, and dynamic models of Hellenic Trench rollback (e.g. Royden & Faccenna 2018). Furthermore, the broad and dispersed distribution of aftershocks appears to indicate that the 2017 earthquake activated many other faults throughout the Gulf and surrounding areas (Fig. 2).

Kurt *et al.* (1999) argue that in the eastern part of the Gulf, south-dipping faults are dominant, while in the west, a north-dipping fault system with a surface expression close to the southern coast of the Datça Peninsula is most prominent (Fig. 2). The seismic sections by Kurt *et al.* (1999) show that at the western part of the Gulf, the sediments are thicker (∼3.5 km) on the southern margin compared to the northern margin (<1 km), which is possibly related to the activity of the north-dipping normal faults with surface expressions near the southern margin of the Gulf. To first order, our result showing that the 2017 event occurred in the western Gulf on a north-dipping fault supports this view.

Karasözen *et al.* (2018) suggested that the fault that ruptured during the 2017 earthquake occurred on the western continuation of the North Datça Fault (Fig. 2). Ganas *et al.* (2019) proposed that the fault that ruptured during the 2017 earthquake followed the Gökova Ridge, which is a 10 km E–W oriented topographic feature 5 km north of the South Datça fault. Whether the coseismic fault connects to the north-dipping South Datça Fault or directly projects to the Gökova Ridge remains to be further explored.

6 CONCLUSIONS

The 2017 Bodrum–Kos Earthquake ruptured the western segment of the Gulf of Gökova. Analyses of the main shock source, GPS and InSAR observations of coseismic deformation and consistency of the early aftershock distribution with the Coulomb stress change due to the coseismic slip distribution, all indicate that the 2017, M_w6.6, Bodrum–Kos earthquake occurred on a ∼40°, north-dipping, 20–25 km long, E–W striking, normal fault, with coseismic slip exceeding 2 m. Our preferred model locates the coseismic fault in the west-central Gulf where it accommodates N–S extension of the Gulf, and serves to separate Kos Island from the Bodrum Peninsula. N–S extension of SW Anatolia is related to the retreat of the easternmost Hellenic Trench that induces backarc, N–S extension and anticlockwise rotation of the Anatolia Extensional Province. The coseismic fault may be an eastward extension of the north-dipping Datça Fault.

ACKNOWLEDGEMENTS

The authors would like to thank the General Directory of Land Registry and Cadaster (TKGM), the General Directory of Mapping (HGM), the Association of Bodrum Geomatic Engineers and Greece NOANET for providing access to their GPS data. Also, the authors thank Mert Gurturk for his contribution at the GPS survey campaign. SAR data are copyrighted by the European Space Agency and were distributed via the Alaska Satellite Facility. We would like to thank two anonymous reviewers for their detailed comments, which helped to improve the this paper significantly.

REFERENCES

Aktug, B. *et al.*, 2009. Deformation of western Turkey from a combination of permanent and campaign GPS data: limits to block-like behavior, *J. geophys. Res.,* **114**(B10404), doi:10.1029/2008JB006000.

Akyol, N., Zhu, L., Mitchell, B., Sözbilir, H. & Kekovalı, K., 2006. Crustal structure and local seismicity in western Anatolia, *Geophys. J. Int.,* **166**(3), 1259–1269.

Bohnhoff, M., Rische, M., Meier, T., Endrun, B., Becker, D., Harjes, H. & Stavrakakis, G., 2004. CYC-NET: a temporary seismic network on the Cyclades (Aegean Sea, Greece), *Seismol. Res. Lett.,* **75**(3), 352–359.

Brüstle, A., 2012. *Seismicity of the Eastern Hellenic Subduction Zone,* Ruhr-University Bochum.

Chen, C. & Zebker, H., 2002. Phase unwrapping for large SAR interferograms: statistical segmentation and generalized network models:, *IEEE Trans. Geosci. Remote Sens.,* **40**(8), 1709–1719.

Emre, O., Duman, T., Dogan, A., Ozalp, S., Tokay, F. & Kuscu, I., 2013. *Active Fault Map of Turkey with an Explanatory Text. 1:1,250,000 Scale,* General Directorate of Mineral Research and Exploration.

Downloaded from https://academic.oup.com/gji/article/219/2/911/5538783 by Yildiz Teknik University Library (YTU) user on 25 February 2022

Farr, T. *et al.*, 2007. The shuttle radar topography mission, *Rev. Geophys.,* **45,** RG2004.

Floyd, M. *et al.*, 2010. A new velocity field for Greece: implications for the kinematics and dynamics of the Aegean, *J. geophys. Res.,* **115**(B110), doi:10.1029/2009JB007040.

Ganas, A. *et al.*, 2017. Co-seismic deformation and preliminary fault model of the July 20, 2017 M6.6 Kos earthquake, Aegean Sea, Tech. Rep.

Ganas, A. *et al.*, 2019. The July 20, 2017 M6.6 Kos earthquake: seismic and geodetic evidence for an active north-dipping normal fault at the western end of the Gulf of Gökova (SE Aegean Sea), *Pure appl. Geophys.*

Gurer, O.F., Sangu, E., Ozburan, M. & Sarica-Filoreau, N., 2013. Complex basin evolution in the Gokova Gulf region: implications on the Late Cenozoic tectonics of the southwest Turkey, *Int. J. Earth Sciences,* **102,** 2199–2221.

Gurolla, E., Agram, P., Lavalle, M., Sacco, G. & Rosen, P., 2016. The InSAR scientific computing environment (ISCE): an earth science SAR processing framework, toolbox, and foundry, *AGU Fall Meeting*.

Görür, N. *et al.*, 1995. Rift formation in the Gökova Region, Southwest Anatolia: implication for the opening of the Aegeran Sea, *Geol. Mag.,* **132,** 637–650.

Heidarzadeh, M., Necmioglu, O., Ishibe, T. & Yalçıner, A., 2017. Bodrum–Kos (Turkey–Greece) Mw 6.6 earthquake and tsunami of 20 July 2017: a test for the Mediterranean tsunami warning system, *Geosci. Lett.,* **4,** 31.

Herring, T., 1998. Documentation for GLOBK: global Kalman filter for VLBI and GPS analysis program, *version 4.1, MIT*.

Herring, T., King, R. & Floyd, M., 2015. *Introduction to GAMIT/GLOBK Release 10.6,* Department of Earth, Atmospheric and Planetary Sciences, MIT.

Ji, C., Wald, D. & Helmberger, D., 2002. Source description of the 1999 Hector Mine, California Earthquake, Part I: wavelet domain inversion theory and resolution analysis, *Bull. seism. Soc. Am.,* **92**(4), 1192–1207.

Karasözen, E. *et al.*, 2018. The 2017 July 20 Mw 6.6 Bodrum–Kos earthquake illuminates active faulting in the Gulf of Gökova, SW Turkey, *Geophys. J. Int.,* **214**(1), 185–199.

Kissling, E., Ellsworth, W., Eberhart-Phillips, D. & Kradolfer, U., 1994. Initial reference models in local earthquake tomography, *J. geophys. Res.,* **99**(B10), 19 635–19 646.

Kurt, H., Demirbag, E. & Kuscu, I., 1999. Investigation of the submarine active tectonism in the Gulf of Gökova, southwest Anatolia–southeast Aegean Sea, by multi-channel seismic reflection data, *Tectonophysics,* **305,** 477–496.

Lienert, B., Berg, E. & Frazer, L., 1986. Hypocenter: an earthquake location method using centred, scaled, and adaptively least squares, *Bull. seism. Soc. Am.,* **76,** 771–783.

McClusky, S. *et al.*, 2000. Global positioning system constraints on plate kinematics and dynamics in the eastern Mediterranean and Caucasus, *J. geophys. Res.,* **105**(B3), 5695–5720.

Ocakoğlu, N., Nomikou, P., İşçan, Y., Loreto, M. & Lampridou, D., 2018. Evidence of extensional and strike-slip deformation in the offshore Gökova-Kos area affected by the July 2017 Mw 6.6 Bodrum-Kos earthquake, eastern Aegean Sea, *Geo-Mar. Lett.,* **38,** 211–225.

Ottemöller, L., Voss, P. & Havskov, J., 2013. Seisan Earthquake analysis software for Windows, Solaris, Linux And Macosx.

Reilinger, R. *et al.*, 2006. GPS constraints on continental deformation in the Africa-Arabia-Eurasia continental collision zone and implications for the dynamics of plate interactions, *J. geophys. Res.,* **111**(B5), B05411.

Rosen, P., Gurolla, E., Sacco, G. & Zebker, H., 2011. *InSAR Scientific Computing Environment (ISCE) – The Home Stretch, Abstract IN42A-02, Paper Presented at AGU Fall Meeting,* San Francisco, CA.

Royden, L. & Faccena, C., 2018. Subduction Orogeny and Late Cenozoic Evolution of the Mediterranean Arcs, *Annu. Rev. Earth Planet. Sci.,* **46,** 261–289.

Royden, L. & Papanikolaou, D., 2011. Slab segmentation and late Cenozoic disruption of the Hellenic arc, *Geochem. Geophys. Geosyst.,* **12**(3).

Saltogianni, V., Taymaz, T., Yolsal-Cevikbilen, S., Eken, T., Gianniou, M., Ocalan, T., Pytharouli, S. & Stiros, S., 2017. *Fault-Model of the 2017 Kos-Bodrum (East Aegean Sea) Mw 6.6 Earthquake from Inversion of Seismological and GPS data—Preliminary Rep.,* Istanbul Technical University.

Sengor, A., Satir, M. & Akkok, R., 1984. Timing of tectonic events in the Menderes Massif, western Turkey: implications for tectonic evolution and evidence for pan-African basement in Turkey, *Tectonics,* **3**(7), 693–707.

Simons, M., Fialko, Y. & Rivera, L., 2002. Coseismic deformation from the 1999 Mw 7.1 Hector Mine, California, earthquake as inferred from InSAR and GPS observations, *Bull. seism. Soc. Am.,* **92**(4), 1390–1402.

Tiryakioğlu, I. *et al.*, 2017. Slip distribution and source parameters of the 20 July 2017 Bodrum-Kos earthquake (Mw 6.6) from GPS observations, *Geodinamica Acta,* **30**(1), 1–14.

Vernant, P., Reilinger, R. & McClusky, S., 2014. Geodetic evidence for low coupling on the Hellenic subduction plate interface, *Earth planet. Sci. Lett.,* **385,** 122–129.

Yalçıner, A. *et al.*, 2017. The 20th July 2017 (22:31 UTC) Bodrum/Kos Earthquake and Tsunami; Post Tsunami Field Survey Rep.

Zhu, L. & Ben-Zion, Y., 2013. Parametrization of general seismic potency and moment tensors for source inversion of seismic waveform data, *Geophys. J. Int.,* **194**(2), 839–843.

Zhu, L. & Helmberger, D., 1996. Advancement in source estimation techniques using broadband regional seismograms, *Bull. seism. Soc. Am.,* **86**(5), 1634–1641.

SUPPORTING INFORMATION

Supplementary data are available at *GJI* online.

BodrumKos_Catalogue

Table S1A. Survey GPS sites derived coseismic displacements.

Table S1B. cGPS stations derived coseismic displacements.

Figure S1. An example of normal fault earthquake and its static deformation. A south-dipping fault is built with constant slip of 3 m between the depths of 2 and 6.5 km. The resulting static deformation is quite symmetric in either direction. (a) The fault plane view of the slip distribution of the synthetic earthquake. The fault plane is dipping north with a dip angle of 40°. (b) The horizontal (the black vectors) and vertical (colours) static displacement due to an earthquake with slip distribution in (a). The blue rectangle shows the fault area projected to the surface. The negative vertical displacements (subsidence) are saturated at −8 cm. The white line shows the profile location of the vertical displacement profile in (c). (c) The vertical displacement perpendicular to the fault plane along the line A–A' shown in (b).

Figure S2. Daily solutions for the GPS time-series from 11 continuous GPS stations of this study. Coseismic displacements obtained from the time-series are shown in Supporting Information Table S1b.

Figure S3. (a) The original interferograms from the from the Copernicus/ESA Sentinel-1 satellite mission ascending track 131 (left) and descending track 036 (right). (b) Detail of unwrapped interferograms of the Bodrum–Kos earthquake. LOS displacement (range change) is plotted. Positive values (the red colours) indicate relative motion away from the satellite; negative values (the blue colours) indicate relative motions towards the satellite. The largest positive displacements in both interferograms are on the southern tip of the island of Karaada, and indicate that it subsided in the earthquake. The Pink star shows the relocated epicentre of this study.

Figure S4. The distribution of the seismic stations used to locate the main shock and aftershocks during the first month following the main shock that are part of KOERI, AFAD, GFZ, INGV and HUSN (the red triangles). The green star shows the epicentre location.

Figure S5. The evolution of the relocated seismicity following the main shock during first 3 d and cumulative seismicity during the first 20 d.

Downloaded from https://academic.oup.com/gji/article/219/2/911/5538783 by Yildiz Teknik University Library (YTU) user on 25 February 2022

Figure S6. Statistics of the relocated aftershocks during the first 20 d following the 2017 July 20 Bodrum–Kos earthquake: (a) latitude, (b) longitude, (c) depth uncertainties and (d) frequency–magnitude distribution and the best-fitting b-value.

Figure S7. Result of an inversion of an M_w4.5 aftershock that occurred a day after the main shock. (a) (left) the best-fitting mechanism information and lower hemispheric projection of station locations. (right) Velocity waveform data (black) and model fits (red) for the *P* waves and *S* and surface wave windows. Station name, distance (km) and azimuth (°) are shown on the left of the traces. A bandpass filter between 0.02 and 0.1 Hz for the 35 s P_{nl} window and 0.02–0.08 Hz for the 70 surface wave window was used. Grid search is performed to obtain the strike, dip and rake angles with 5° intervals and to the moment magnitude for a step size 0.1. Maximum time-shifts were chosen as 2 and 5 s for the P_{nl} and surface wave components, respectively. Station name, distance and azimuth of each station are shown on left of the waveforms. (b) Depth versus variance reduction and the best-fitting mechanism at each depth.

Figure S8. Bootstrap analysis of selected aftershocks with a variance reduction of ∼50 per cent. The date, time and magnitude of each earthquake are indicated at the top of the histograms for strike, dip and rake, respectively. By fitting a Gaussian curve, the average value (μ) and the standard deviation (σ) from the bootstrap analysis is calculated and displayed on top right of each plot. Strike, dip and rake values using all the data are also listed below the bootstrap results.

Figure S9. Results of the grid search for finding the location of the best-fitting fault plane for the (a) north-dipping fault (strike 285°, dip = 39°), (b) south-dipping (strike = 84°, dip = 53°). Each circle represents a finite-fault model where the location of the circle represents the centre point along strike and 6 km depth .The x_r^2error values are saturated at 7.0 for both figures.

Please note: Oxford University Press is not responsible for the content or functionality of any supporting materials supplied by the authors. Any queries (other than missing material) should be directed to the corresponding author for the paper.

Downloaded from https://academic.oup.com/gji/article/219/2/911/5538783 by Yildiz Teknik University Library (YTU) user on 25 February 2022